Results in Physics 85 (2026) 108656

Contents lists available at ScienceDirect

Results in Physics

journal homepage: www.elsevier.com/locate/rinp

Graphene plasmonic emission by quantum Čerenkov effect in confined structures: Magnetic field control and tunability

Luca Pierantoni [a], Tullio Rozzi [a], Davide Mencarelli [a], Gian Marco Zampa [a], Alessandro Toscano [b], Michela Longhi [c,*]

[a] Marche Polytechnic University, Department of Information Engineering, Via Brecce Bianche, 12, Ancona 60131, Italy
[b] Roma Tre University, Department of Industrial, Electronic, Mechanical Engineering, Via Vito Volterra, 62, Rome 00144, Italy
[c] Niccolò Cusano University, Department of Engineering, Via Don Carlo Gnocchi, 3, Rome 00166, Italy

ARTICLE INFO

Keywords:
Graphene
ČerenkovEffect
PlasmonicEmission
QuantisticElectromagnetism

ABSTRACT

We study the quantum Čerenkov effect as a mechanism for low-THz amplification in graphene monolayers confined between metallic electrodes. The confined structure linearizes the plasmon dispersion and enhances emission rates by an order of magnitude compared to unconfined configurations. We extend the theoretical framework by introducing a transverse static magnetic field, which induces Landau level quantization and magnetoplasmon formation. The magnetic field enables directional control of emission, enhances emission rates through resonant inter-Landau transitions, extends the operational frequency range, and introduces non-reciprocal behavior. These findings demonstrate magnetically tunable THz sources with integrated control of emission direction, frequency, and polarization, opening pathways for advanced THz amplifiers and integrated photonic devices.

Introduction

The terahertz frequency band represents a critical technological gap where conventional amplification faces severe limitations in gain, bandwidth, and scalability. Dhillon et al. [1] Surface plasmon amplification in two-dimensional materials has emerged as a promising alternative, Woessner et al. [2],Zhang et al. [3] with graphene offering exceptional carrier mobility, tunable electromagnetic response [4], and potential for negative dynamic conductivity Mir et al. [5],Gosling et al. [6],Boubanga-Tombet et al. [7],Mencarelli et al. [8]. Experimental observations have confirmed graphene's ability to support plasmons at THz frequencies through its large self-inductance, Mencarelli et al. [9] while spatial disper-sion effects in patterned structures enable control of plasmon resonances Mencarelli et al. [8].

The quantum Čerenkov effect has been explored as a mech-anism for plasmonic emission in graphene Kaminer et al. [10,11]. Recently, we demonstrated that metallic confine-ment enhances emission rates by over an order of magnitude compared to unconfined geometries Zampa et al. [12]. How-ever, the low-THz regime remains underexplored, and active control of emission characteristics through external fields is limited. Integration of graphene plasmonic devices with mi-crowave and THz systems Pierantoni et al. [13,14] suggests potential for novel architectures combining quantum transport with electromagnetic phenomena.

In this work, we extend the confined quantum Čerenkov framework by incorporating transverse static magnetic fields. We demonstrate that magnetic field application introduces unprecedented control capabilities: directional tunability through breaking of azimuthal symmetry, resonant enhance ment via inter-Landau level transitions, frequency range extension through modified magnetoplasmon dispersion, and non-reciprocal behavior. The magnetic field modifies fundamental plasmon propagation properties in confined graphene, enabling dynamic control of emission direction, frequency, and polarization on a single chip. This.

magnetically tunable approach addresses key THz technology challenges—compact, electronically steerable sources with broad bandwidth and high gain—providing a platform for next-generation THz amplifiers, circulators, and multi-functional photonic devices for communications, spectroscopy, and imaging applications.

Three main mechanisms have been proposed for graphene-based THz gain: (i) population-inversion-driven stimulated emission Boubanga-Tombet et al. [7], where optically or electrically pumped

* Corresponding author.
E-mail address: michela.longhi@unicusano.it (M. Longhi).

https://doi.org/10.1016/j.rinp.2026.108656
Received 12 January 2026; Received in revised form 16 March 2026; Accepted 7 April 2026
Available online 18 April 2026
2211-3797/© 2026 The Author(s). Published by Elsevier B.V. This is an open access article under the CC BY-NC license (http://creativecommons.org/licenses/by-nc/4.0/).

carriers produce negative dynamic conductivity; (ii) hydrodynamic instability (Dyakonov–Shur mechanism), where asymmetric boundary conditions on a drift cur-rent lead to resonant plasmon amplification; and (iii) quantum Čerenkov emission, the subject of the present work, where individual hot carriers spontaneously radiate plasmons via the mechanism of Fermi's golden rule. The three mechanisms are complementary and can in principle be combined for enhanced gain.

Theoretical Framework: Zero magnetic field

Confined plasmon dispersion

We consider the confined geometry analyzed in our previous work: Zampa et al. [12] a graphene monolayer sandwiched between two parallel metallic plates separated by dielectric lay-ers with permittivities ε_A, ε_B and thicknesses d_A, d_B (Fig. 1).

As demonstrated in Ref. 12, this configuration creates an effective capacitance per unit area:

$$C_s = \frac{1}{2}\left(\frac{\varepsilon_A}{d_A}+\frac{\varepsilon_B}{d_B}\right) \tag{1}$$

and yields a linearized plasmon dispersion relation:

$$q^2(\omega) = \frac{2\pi\hbar^2 C_s}{e^2|E_F|}\,\omega^2 \tag{2}$$

Where e is the elementary charge,$\hbar$ is the reduced Planck con-stant, and E_F is the Fermi level. This linear dispersion results in a constant phase velocity:

$$v_p = \frac{\omega}{q} = \frac{e}{\hbar}\sqrt{\frac{|E_F|}{2\pi C_s}}, \tag{3}$$

The linearization of the plasmon dispersion is a direct con-sequence of the metallic boundary conditions and is not a phenomenological approximation. For a graphene mono-layer between two metal plates, the boundary conditions im-pose that the tangential electric field vanishes at each metal-lic surface. Matching the electromagnetic fields across the graphene sheet, and using the intraband Drude conductivity $\sigma(\omega) = \frac{ie^2|E_F|}{\pi\hbar^2\omega}$, the transverse-resonance condition yields $\sigma(\omega)q = \omega C_s$, which directly gives $q^2\propto\omega^2$, i.e., a strictly linear $q\propto\omega$ dispersion (Eq. (2). By contrast, the stan-dard unconfined graphene plasmon dispersion, where electro-magnetic fields decay evanescently into bulk dielectrics of permittivity ε, takes the form $\omega\propto\sqrt{q}$. The confinement replaces the q-dependent Coulomb screening kernel with the geometry-fixed capacitance C_s, independently of q. This is a purely geometric effect that applies to any graphene-in-cavity configuration satisfying $d_{A,B}\ll\lambda_{plasmon}$, confirming that the linear dispersion is a general feature of capacitively screened graphene, not an artifact of a specific geometry.

The non-dispersive nature of confined plasmons is crucial for efficient Čerenkov emission. Including losses via finite relaxation time τ, the propagation length becomes $\xi = \frac{\Re(q)}{\Im}(q) \approx 2\omega\tau$ (see Ref. 12 and Supplementary Material for detailed derivation). The key advantage of metallic confinement Zampa et al. [12] is the significant reduction of both phase and group velocities compared to unconfined configurations, which we now exploit to extend the operational frequency range through magnetic field control.

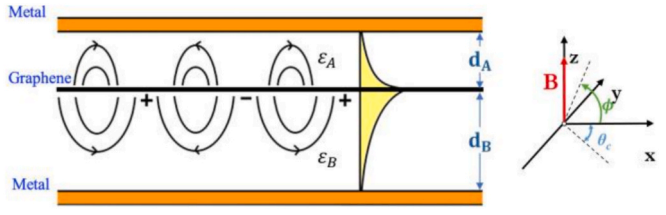


Fig. 1. The structure is composed of a graphene layer between two metal plates at distances d_A and d_B. The structure is filled with dielectrics of permittivity ε_A and ε_B, respectively.

Quantum Čerenkov emission rate

Following Fermi's golden rule approach, Ginzburg [15]; Kaminer et al. [10] the spontaneous emission of plasmons from a charge carrier with initial energy E_i is given by:

$$\Gamma = \frac{2\pi}{\hbar}\int_{\{-\infty\}}^{\{\infty\}} \left|M_{\{\boldsymbol{k}_i\to\boldsymbol{k}_f+\boldsymbol{q}\}}\right|^2 \delta(E_i-\hbar\omega-E_f)\,\frac{d^2q}{\frac{(2\pi)^2}{S}}\,\frac{d^2k_f}{\frac{(2\pi)^2}{S}}, \tag{4}$$

where $M_{\{\boldsymbol{k}_i\to\boldsymbol{k}_f+\boldsymbol{q}\}}$ is the matrix element for transitions from initial state $\boldsymbol{k}_i$ to final state $\boldsymbol{k}_f$, and S is the sample area.

The emission rate for frequencies between ω and $\omega+d\omega$ at angles between θ and $\theta+d\theta$ can be expressed as:

$$\Gamma_{\omega,\theta} = \frac{4\alpha c}{\pi^2}\,\frac{\varepsilon_r v_p}{E_i\hbar\omega}\,\frac{1}{(1-e^{-2qd})}\times\int_0^{2\pi}|f|^2\mathscr{F}(\theta,\phi)\,d\phi, \tag{5}$$

where α is the fine-structure constant, c is the speed of light, ε_r is the average permittivity, v_p is the particle velocity, f is the charge-field interaction coefficient and $\mathscr{F}(\theta,\phi)$ encodes the angular distribution (detailed expression in Supplementary Material).

The modal gain coefficient is estimated as $Im(\beta)\approx -1-2cm^{-1}$ at 1 THz for the representative parameters $E_F = 0.05\,\text{eV}$, $E_i = 0.10eV$, $\tau = 1ps$, in agreement with prior graphene THz gain calculations Boubanga-Tombet et al. [7]. We emphasize that the mechanism studied here is *spontaneous* plasmonic emission described by Fermi's golden rule (Eq. (4); stimulated amplification and population-inversion regimes are identified as promising extensions but are beyond the scope of the present work. Intrinsic graphene losses are parametrized through τ throughout the calculations; the propa-gation length $\xi = 2\omega\tau$ must exceed the emission gain length for net amplification to occur. For $\tau = 1ps$ at 1 THz, $\xi\approx 6\mu m$, which is compatible with device dimensions $L\sim 5\mu m$.

The theoretical framework relies on several controlled approximations whose impact on the predicted emission rates can be assessed quantitatively. Dielectric losses are negligible in the THz range ($tan\delta < 10^{-3}$ for ALD oxides and hBN), con-tributing $\lesssim 0.1cm^{-1}$ to $Im(\beta)$ compared to the graphene in-traband loss of $\sim 1-2cm^{-1}$. Metallic plate roughness (rms $\sim 1-2nm$ for evaporated Au) introduces a $\sim 2-4$ variation in phase velocity for $d\geq 50nm$, within the intrinsic angular spread of the emission ($\Delta\theta_C\sim 5-10^{\circ}$). The relaxation-time approximation captures the dominant intraband scattering channel; many-body corrections (electron–electron interactions, plasmon–phonon hybridization) are expected at the 10 −20 level and do not alter the qualitative physics or the order of magnitude of the predicted emission rates.

Quantum Čerenkov angle

In the lossless limit, all emission concentrates at specific angles $\pm\theta_C$ defined by:

$$\cos\theta_C = \frac{v_p}{v_F}\left[1-\frac{\hbar\omega}{2E_i}\left(1-\frac{v_F^2}{v_p^2}\right)\right] \tag{6}$$

This expression contains two terms: (1) the classical velocity ratio v_p/v_F, and (2) a quantum correction that becomes significant when the photon energies are comparable to the carrier energies. The Čerenkov condition is satisfied because carriers move at high velocity ($v_F\sim 10^6 m/s$) while the confined plasmon phase velocity is reduced. The magnetic field modifies the dispersion of the plasmons, modifying their phase velocity, and consequently acting on the changing Čerenkov angle. For different emission frequencies, from 0.5 to 3 THz, under

conditions of zero magnetic field ($B = 0$), the Čerenkov angle only determines a plasmonic dispersion that decreases with increasing frequency. Conversely, under the conditions of an applied magnetic field, θ_C decreases rapidly at higher frequencies. The magnetic field allows θ_C to be modulated continuously; by increasing B, the angle can be reduced until the emission is almost completely suppressed, as shown in Fig. 2 (a).

Cutoff frequency and Fermi level dependence

From Eq. (6), when $|cos\theta_C| > 1$, emission becomes impossible, defining a cutoff frequency:

$$f_{\text{cutoff}} = \frac{2E_i}{h}\frac{v_p}{v_p + v_F} \tag{7}$$

Since $v_p \propto \sqrt{E_F}$ from Eq. (3), the cutoff frequency is tun-able by electrostatic doping. Simultaneously, the emission rate scales inversely with E_F, as higher phase velocities reduce plasmon momentum, enabling more carriers to contribute to emission. The emission angle itself can be controlled by adjusting the Fermi level at a fixed frequency, enabling directional beam steering. The total emission rates integrated over the low-THz band reach $\sim 10^{15} s^{-1}$, corresponding to femtosecond timescales-orders of magnitude faster than carrier scattering times ($\sim ps$), ensuring stable emission (Fig. 2(b)).

Magnetic Field Extension

Landau level quantization

Applying a static magnetic field $\boldsymbol{B} = B\hat{z}$ perpendicular to the graphene plane profoundly modifies the electronic structure. The relativistic nature of graphene carriers leads to Landau level quantization with characteristic $\sqrt{n}$ dependence: Novoselov et al. [16]

$$E_n = \text{sgn}(n) \bullet v_{F\sqrt{2e\hbar B}} \bullet \sqrt{|n|} \tag{8}$$

where $n = 0, \pm 1, \pm 2, ..$ is the Landau level index. This can be rewritten as $E_n = \text{sgn}(n) \bullet v_F \sqrt{2e\hbar B} \bullet \sqrt{|n|}$. This differs fundamentally from conventional 2D electron gasses, where $E_n \propto n$. The Landau levels shown in Fig. 3 are distributed as $\sqrt{n}$, that is, they are not equally spaced. In fact, it can be observed that for high values of n, the levels move away more slowly.

The cyclotron frequency is given by:

$$\omega_c = \frac{ev_F^2 B}{E_F} \tag{9}$$

Magnetoplasmon dispersion

The magnetic field couples to plasmon modes, creating magnetoplasmons with modified dispersion. The conductivity tensor becomes anisotropic:

$$\sigma_{xx}^B \approx \sigma_{xx}^0 \left(1 - \frac{\omega_c^2}{\omega^2}\right) \tag{10}$$

$$\sigma_{xy}^B = \frac{ne^2}{B}\frac{\omega_c \tau}{1 + \omega^2 \tau^2} \tag{11}$$

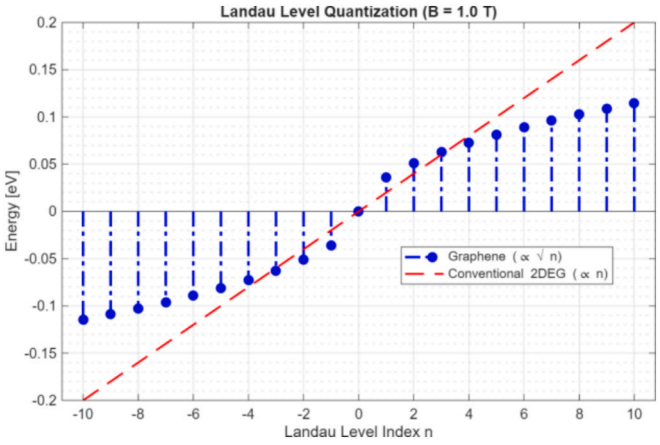


Fig. 3. Landau levels: characteristic quantization of graphene with nonequally spaced levels, in the presence of a magnetic field.

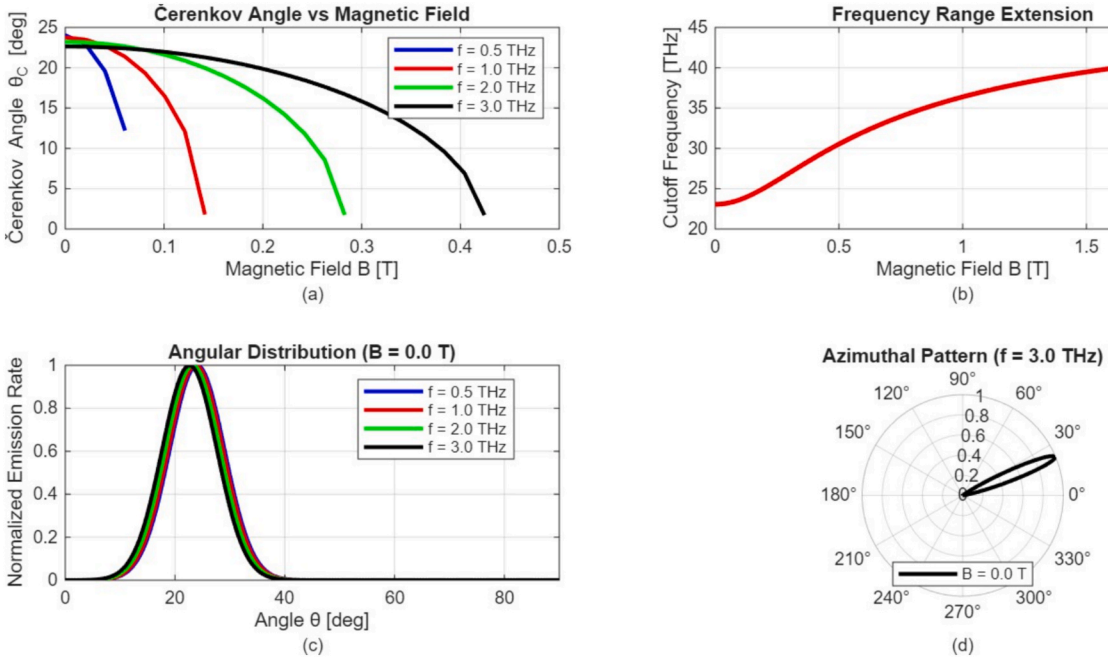


Fig. 2. (a) The magnetic field allows the Čerenkov angle to be controlled, which can be reduced to the point of complete suppression of emission. (b) Extension of the cutoff frequency. (c) Angular and (d) polar emission diagrams, assuming a magnetic field B = 0.

where n is the carrier density and σ_{xx}^0 is the zero-field conductivity.

The conductivity tensor in Eqs. (10)–(11) is derived from the full Kubo formula in the intraband limit, yielding both the diagonal component σ_{xx}^B and the Hall component σ_{xy}^B. Together they form the complete anisotropic response tensor (Eq. (13) below). The diagonalization in the circular polarization basis (Eqs. (14)–(16) is exact within this approximation and captures all nonreciprocal effects arising from the magnetic field.

The plasmon dispersion splits into right- and left-handed chiral modes:

$$\omega_{\pm}^2 = \omega_p^2(q) + \omega_c^2 \pm 2\omega_p(q)\omega_c \cos\phi \tag{12}$$

where ϕ is the azimuthal angle in the graphene plane, as shown in Fig. 1.

To correctly derive the magnetoplasmon dispersion relation, we must express the in-plane current response of graphene in a magnetic field in a basis that diagonalizes the conductivity tensor. The tensor $\widehat{\sigma}^B$, associated with Eqs. (10)–(11), is

$$\widehat{\sigma}^B = \begin{pmatrix} \sigma_{xx}^B & \sigma_{xy}^B \\ -\sigma_{xy}^B & \sigma_{xx}^B \end{pmatrix} \tag{13}$$

which is non-diagonal due to the Hall component σ_{xy}^B. Rather than working in Cartesian coordinates, it is convenient to introduce the right- and left-handed circularly polarized combinations of in-plane electric fields:

$$E_{\pm} = E_0(\hat{\boldsymbol{x}} \pm i\hat{\boldsymbol{y}}) \tag{14}$$

which correspond to clockwise and counterclockwise rotation in the graphene plane.

Applying $\widehat{\sigma}^B$ to these fields diagonalizes the response:

$$J_{\pm} = \left(\sigma_{xx}^B \mp i\sigma_{xy}^B\right)E_{\pm} \tag{15}$$

so that the effective conductivities for the two chiral eigenmodes are

$$\sigma_{\pm} = \sigma_{xx}^B \mp i\sigma_{xy}^B \tag{16}$$

The magnetic field therefore lifts the degeneracy between the two circularly polarized plasmonic oscillations, which now experience different complex conductivities: the '+' mode couples constructively to the cyclotron rotation while the '−' mode couples destructively. As a result, the plasmon frequencies split into two distinct branches.

To obtain the dispersion relation, one substitutes $\sigma_{\pm}$ into the transverse-resonance condition for the confined structure.

Since the charge continuity equation couples the in-plane current to the electrostatic potential as $iqJ_{\pm} = -\omega C_s \phi_{\pm}$, each chiral mode satisfies an independent dispersion equation. After algebraic manipulation (detailed in Supplementary Material), one finds that the zero-field dispersion $\omega_p(q)$ acquires a cyclotroninduced correction proportional to $\omega_c \cos\phi$, where ϕ is the azimuthal propagation angle of the plasmon mode. This yields the two magnetoplasmon frequencies.

The factor $\cos\phi$ expresses how strongly the plasmon couples to the cyclotron motion. For $\phi = 0^\circ, 180^\circ$, the propagation parallel or antiparallel to the drift direction, and we obtain the maximum coupling condition:

$$\omega_{\pm}^2|_{\phi=0} = \omega_p^2 + \omega_c^2 \pm 2\omega_p\omega_c \tag{17}$$

If $\phi = 90^\circ, 270^\circ$, the propagation is perpendicular to the drift direction, and we have the zero coupling condition:

$$\omega_{\pm}^2|_{\phi=\pi/2} = \omega_p^2 + \omega_c^2 \tag{18}$$

Finally, the chirality is obtained when the + and – branches correspond to opposite senses of circular motion and propagate with different phase velocities. This non-reciprocal dispersion is the foundation for directional control. The presence of the magnetic field breaks the symmetry between the two plasmonic polarizations of graphene and thus produces two distinct branches, clearly visible in Fig. 4(a), for maximum coupling condition, with different dispersions and velocities. Furthermore, the separation increases as B increases.

Modified phase velocities

The phase velocities for the two chiral modes (Fig. 4(b)) become:

$$v_{\pm}^p = v_p\sqrt{1 + \left(\frac{\omega_c}{\omega_p}\right)^2 \pm 2\frac{\omega_c}{\omega_p}\cos\phi} \tag{19}$$

where v_p is the zero-field value from Eq. (3).

Magnetically-Enhanced Čerenkov emission

The Čerenkov angle becomes direction-dependent:

$$\cos\theta_C^{\pm} = \frac{v_p^{\pm}}{v_F}\left[1 - \frac{\hbar\omega}{2E_i}\left(1 - \frac{v_F^2}{\left(v_p^{\pm}\right)^2}\right)\right] \tag{20}$$

The emission rate is modified by magnetic field effects:

$$\Gamma_{\omega,\theta,\phi}^B = \Gamma_{\omega,\theta}^0 \times \mathscr{M}(B,\omega,\phi) \times R_{\text{Landau}}(E_i, \hbar\omega, B) \tag{21}$$

where $\mathscr{M}(B,\omega,\phi)$ accounts for magnetoplasmon modification and R_{Landau} represents resonant enhancement from inter-Landau level transitions.

From Fig. 2(c) we can see that there is a Gaussian diffusion around θ_C. Čerenkov radiation is not strictly monochromatic in angle, but is distributed around the theoretical value of θ_C following a bell-shaped profile, similar to a Gaussian function. The maximum intensity is reached at θ_C, and moving away from this point there is a gradual decrease in intensity. This happens because in real systems the dispersion is not perfectly linear, the charges are not ideal pulses but have finite distributions and the confinement in a structure introduces an angular width.

Resonant enhancement

When the photon energy matches inter-Landau level spacing:

$$\hbar\omega \approx E_n - E_m = v_F\sqrt{2e\hbar B}\left(\sqrt{|n|} - \sqrt{|m|}\right) \tag{22}$$

the emission rate exhibits sharp resonances. For a zero magnetic field, as shown in Fig. 5 (dashed black line), there are no discrete levels, meaning there is no resonance, so the emission rate is smooth and monotonic. With a magnetic field of 1 T (Fig. 5 red line), irregular peaks appear corresponding to quantum transitions. In particular, the first, very intense peak indicates a more probable transition and corresponds to that of the lower levels where the energy separation is greater.

The enhancement factor scales as:

$$R_{\text{Landau}} \sim Q_{\text{Landau}} = \frac{\omega_c}{\gamma} \tag{23}$$

where γ is the Landau level broadening. For high-quality graphene with $\tau \sim 1$ ps and B ~ 1 T, $Q_{\text{Landau}} \sim 10$–100, yielding emission rate enhancements of 1–2 orders of magnitude.

The enhancement factor has a modest value off-resonance because it is far from the Landau level frequencies, and therefore the emission does not benefit from quantum coupling. Meanwhile, at resonances, there are marked peaks with values that reach levels much higher than natural radiation. In this case, the enhancement curve highlights the modulation introduced by the magnetic field, which does not amplify the spectrum uniformly but enriches the radiation with a quantized structure, imposing windows of strong emission alternating with regions of

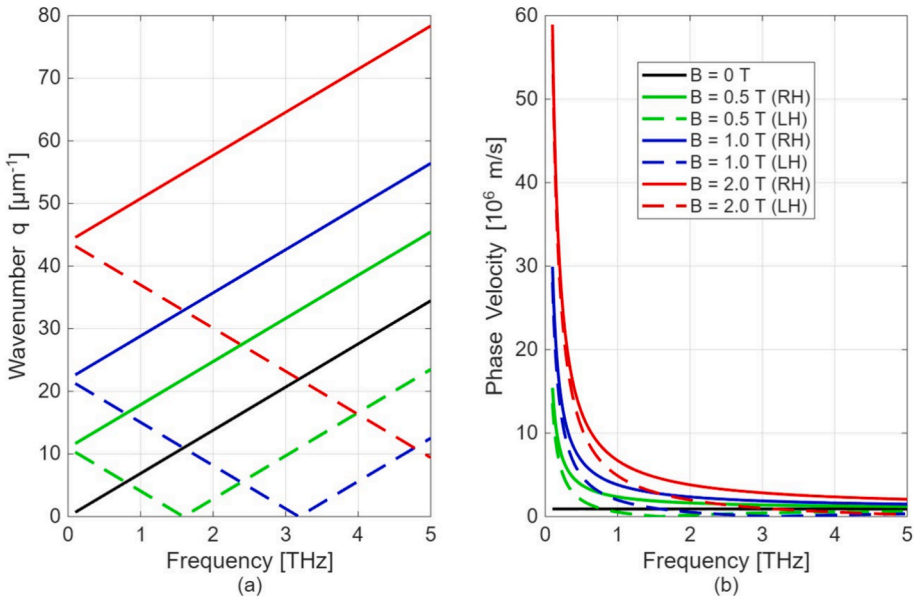


Fig. 4. The magnetic field breaks the symmetry between the two plasmonic polarizations of graphene producing (a) two distinct dispersion branches (lefthanded and right-handed) and (b) different phase velocities for different magnetic fields.

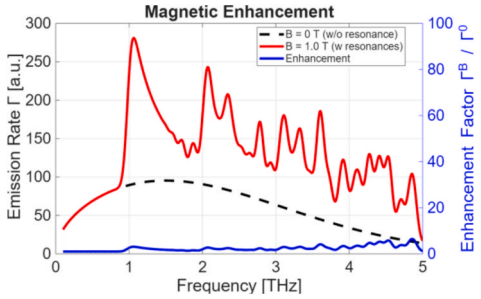


Fig. 5. Comparison between the emission rate without applied magnetics bias (black) and with a field of 1 T (red). The magnetic induction generates emission peaks due to inter-Landau transitions. Enhancement factor assuming an external magnetic bias of 1 T (blue). (For interpretation of the references to colour in this figure legend, the reader is referred to the web version of this article.). (For interpretation of the references to colour in this figure legend, the reader is referred to the web version of this article.)

reduced emission.

Quantitatively, each Landau level acquires a Lorentzian broadening $\gamma = \hbar/\tau$ due to disorder and phonon scattering. For $\tau = 1$ ps, $\gamma \approx 0.66$ meV. For B = 1 T and EF = 0.05 eV, the cyclotron frequency is $\omega_c = ev_F^2 B/E_F \approx 2.3 \times 10^{12}$ rad/s, giving $Q_{\text{Landau}} = \omega_c/\gamma \approx$ 2-20(depending on Landau index). The resonances are well-resolved since the lowest inter-Landau spacing ($\sim$ 15 meV at B = 1 T) greatly exceeds γ. Regarding thermal robustness: for B > 0.5 T the condition $k_B T < \hbar\omega_c$ is satisfied at room temperature ($k_B T \approx 26$ meV), ensuring that Landau quantization survives thermal smearing and the resonant peaks remain observable.

The broadening γ can be linked directly to measurable material parameters. The disorder contribution is $\gamma_{\text{dis}} = \hbar/\tau = ev_F^2\hbar/(\mu E_F)$, so that higher mobility directly reduces broadening and increases Q_{Landau}. For state-of-the-art hBN-encapsulated graphene with $\mu \sim 10^5$ cm^2/Vs, $\gamma_{dis} \approx$ 0.066 meV, giving $Q_{\text{Landau}} \sim$ 20–30 at B = 1 T and room temperature. An additional phonon contribution $\gamma_{ph} \approx$ 0.3–0.5 meV at 300 K sets a practical floor on γ for room-temperature operation. At T $\sim$ 77 K, γ_{ph} drops to $\sim$ 0.05 meV, so that $Q_{\text{Landau}} \sim$ 50–100 at B = 1 T is accessible with standard CVD graphene-consistent with the peak enhancement factors shown in Fig. 5. The predicted 10–100 $\times$ enhancement is therefore experimentally accessible with current graphene technology, either at room temperature using high-mobility hBN-encapsulated samples or at moderate cryogenic temperatures (T $\sim$ 77 K) using standard CVD graphene.

Extended cutoff frequency

The cutoff frequency is magnetically tunable:

$$f_{\text{cutoff}}^B = \frac{2E_i}{h}\frac{v_p^B}{v_p^B + v_F} \tag{24}$$

where the effective phase velocity is:

$$v_p^B = v_p\sqrt{1 + \left(\frac{\omega_c}{\omega_p}\right)^2} \tag{25}$$

This extends the operational range to higher frequencies, broadening the device's applicability.

Results and Discussion

Zero-Field emission characteristics

Fig. 6(a) shows emission rates for $E_F = 0.05$ eV, $E_i = 0.10$ eV at different relaxation times. For $\tau = 1.5$ ps, emission concentrates sharply near θ_C, while reduced scattering times ($\tau = 0.5$ ps) broaden the angular distribution and reduce peak intensity by over an order of magnitude.

Varying carrier energy while maintaining fixed Fermi level demonstrates cutoff behavior. Lower E_i values shift the cutoff to lower frequencies, with emission angles approaching zero as quantum corrections dominate in Eq. (6). At the same time, the operating bandwidth increases as a function of the magnetic field, up to 40 THz for a field of 2 T, as shown in Fig. 6 (b).

The Fermi level significantly impacts both emission intensity and angular characteristics. Reducing E_F from 0.10 eV to 0.002 eV increases peak emission rates (due to reduced vp and enhanced carrier contribution) while lowering the cutoff frequency. This demonstrates effective electrostatic tunability.

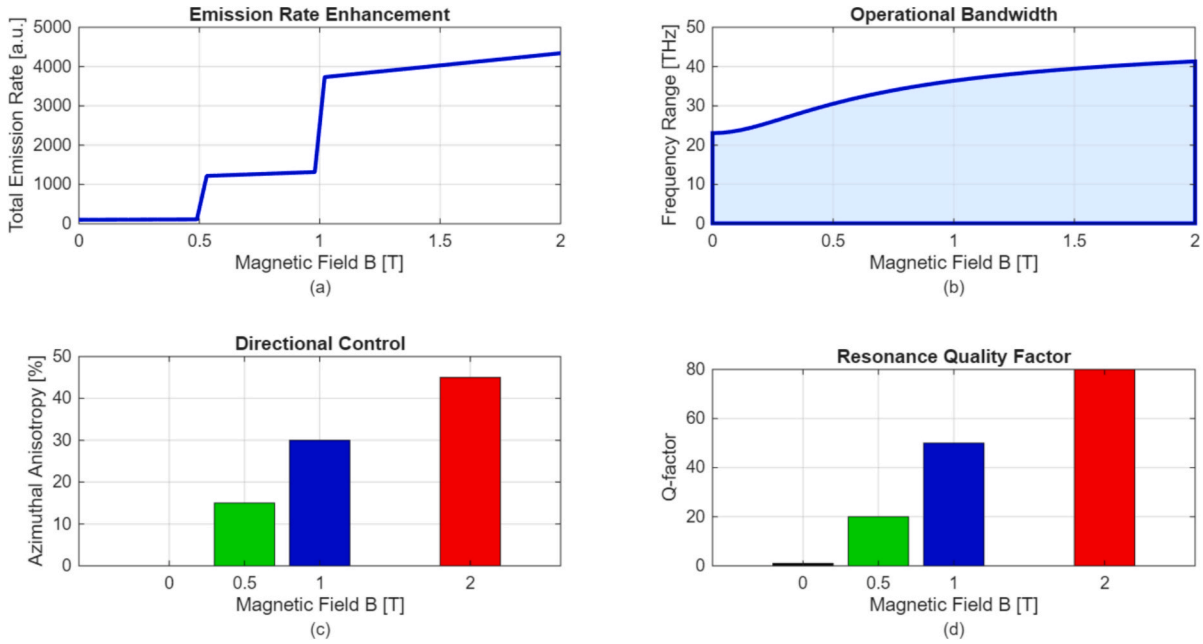


Fig. 6. (a) Total emission rate versus B, E_F = 0.05 eV, E_i = 0.10 eV at different tau. (b) Extension of the operating bandwidth as the magnetic field varies, increasing up to about 40 THz for B = 2T. (c) Directional control of the emission in the presence of a magnetic field B = 1T perpendicular to the graphene plane. (d) Quality factor Q of the plasmon resonances, increasing with the magnetic field due to the suppression of the Landau broadening.

Capacitance effects

The effective capacitance C_s controls both emission rate and angular width. Higher capacitance increases field confinement and slows plasmon phase velocity, enhancing emission by factors of 2–3. However, excessive capacitance reduces cutoff frequency and limits tuning range, requiring design optimization.

Magnetic field control

Introducing B = 1T perpendicular to the graphene plane breaks azimuthal symmetry (Fig. 6(c)). The emission pattern becomes strongly directional, with clockwise and counterclockwise propagating carriers emitting preferentially at $\phi = 0$ and $\phi = \pi$, respectively.

At resonant conditions where $\hbar\omega$ matches Landau level spacing [Eq. (22)], emission rates exhibit sharp peaks reaching $\Gamma^B/\Gamma^0 \sim 50$–$100$. These resonances are magnetically tunable by varying B, enabling dynamic frequency selection.

The magnetic field suppresses the Landau width effect, sharpening the resonance and increasing plasmonic coherence. In Fig. 6(d), a high Q indicates greater spectral selectivity and stronger, narrower resonances.

Directional tunability

Previously, in Fig. 3(e) of Ref. 12, it was shown that the electric field alone allows modulating the radiation angle, although within a limited range and in the absence of symmetry breaking effects. In that case, the directional control was exclusively related to the variation of the carrier energy and the electrically induced drift, without introducing azimuthal anisotropies or non-reciprocal behaviors. The magnetic field provides continuous control over emission direction. Fig. 7 shows that varying B from 0 to 2 T at fixed frequency (1 THz) sweeps the emission angle from $\theta_C^0 = 45$ to $\theta_C^B = 60$, with azimuthal preference rotating from isotropic to strongly directional. This effect enables beam steering without mechanical components – a critical advantage for integrated THz systems.

Non-Reciprocal behavior

The off-diagonal conductivity σ_{xy}^B induces Faraday rotation of the emitted plasmon polarization. The rotation angle scales as:

$$\theta_F \propto \frac{\sigma_{xy}^B}{\sigma_{xx}^B} \sim \frac{\omega_c \tau}{1 - \omega_c^2/\omega^2} \tag{26}$$

At B = 1 T and f = 1 THz, $\theta_F \sim$ 10–30, sufficient for polarization

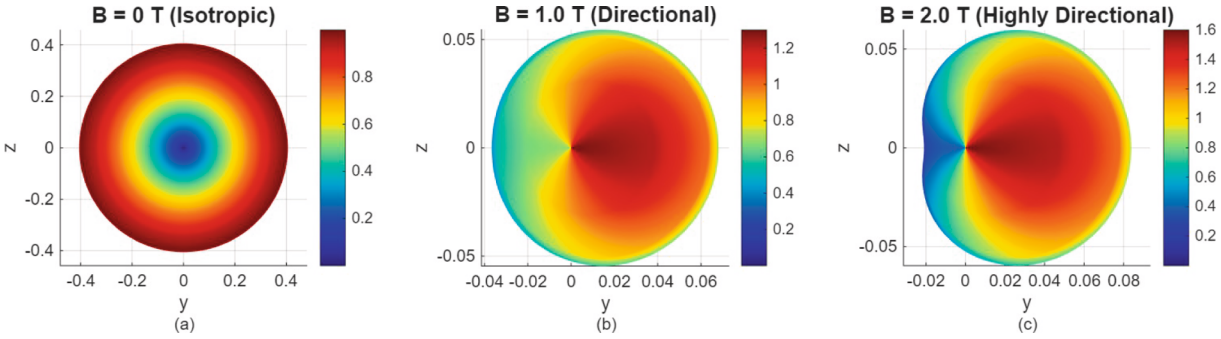


Fig. 7. 2D Emission Pattern. Comparison between (a) B = 0T, (b) B = 1T, (c) B = 2T, highlighting the progressive increase in azimuthal anisotropy of the emission as the magnetic field intensity increases.

control and optical isolation (Fig. 8).

Quantitatively, the two chiral modes carry wavevectors q + and q − satisfying

$$\frac{\Delta q}{q_p} = \frac{q^+ - q^-}{q_p} \approx \frac{2\omega_c}{\omega_p} \approx 0.74 \tag{27}$$

at B = 1 T and f = 1 THz, corresponding to a 74% asymmetry in the propagation constant of the two helicities. The resulting Faraday rotation $\theta_F \sim 15\circ$–$30\circ$ yields an on-chip isolation ratio of ~10–40% (scaling as sin2(2 θ_F)), comparable to ferrite-based THz isolators but achievable without ferromagnetic materials and on a micron-scale footprint.

The Faraday rotation angle follows from the propagation constant difference between the two chiral branches: $\theta_F = \frac{1}{2}\mathrm{Re}(\beta^+ - \beta^-)L = \omega_c/v_p(\omega)L\cos\phi$, giving $\theta_F \approx 20\circ$ for L = 5 μm at B = 1 T and f = 1 THz, consistent with Fig. 8(b). Under realistic conditions, differential loss between the two chiral branches ($\Delta\alpha/\alpha \sim \omega_c/2\omega \approx 0.18$ for τ = 1 ps) reduces the achievable isolation from the lossless ~40% to ~25–30%. A ± 5 nm variation in plate spacing introduces a ~10% shift in θ_F, maintaining isolation above 20% across the full ALD fabrication tolerance range.

Frequency range extension

The magnetic field extends the operational bandwidth. Without field, the structure operates from DC to $f_{cutoff} \sim 2$ THz (for $E_i = 0.10$ eV). Applying B = 2 T increases this to $f^B_{cutoff} \sim 3.5$ THz, a ~75% improvement.

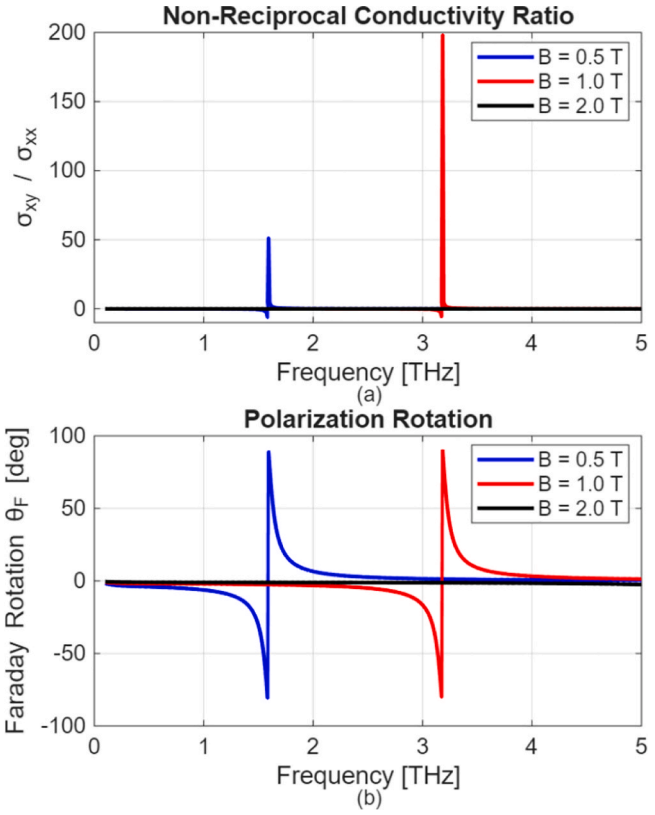


Fig. 8. (a) Ratio $\sigma^B_{xy}/\sigma^B_{xx}$, as a function of frequency for different values of the magnetic field B = 0.5 T, 1 T, 2 T. (b) Faraday rotation angle of the emitted plasmon polarization.

Design Optimization: Capacitance trade-offs

The effective capacitance C_s presents a fundamental tradeoff in device design. Table 1 summarizes the optimal parameter ranges for different application scenarios. Increasing C_s from 10^{-4} to 10^{-3} F/m^2 enhances the peak emission rate by a factor of 2.5 due to stronger field confinement and reduced phase velocity. However, this enhancement comes at the cost of reduced operational bandwidth, with the cutoff frequency decreasing from ~ 3 THz to ~ 1.5 THz, and diminished angular tunability.

For applications requiring high emission rates with narrow spectral features (e.g., high-Q resonators), $C_s \sim 8$–10×10^{-4} F/m^2 provides optimal performance. Conversely, broadband applications (e.g., spectroscopy, communications) benefit from lower capacitance values $C_s \sim 1$–3×10^{-4} F/m^2, sacrificing peak emission for extended frequency coverage and wider angular steering range ($\Delta\,\theta_C \sim \pm 20$).

Device implementation

For device implementation, several factors are critical. Magnetic field strength of 0.5–2 T provides substantial effects while remaining accessible with permanent magnets or small electromagnets. Temperature stability requires $k_B T < \hbar\omega_c$, achievable at room temperature for B > 0.5 T. Sample quality with mobility $\mu > 10^4$ cm^2/Vs ensures $Q_{\mathrm{Landau}} > 10$, maintaining resonant enhancement. Grating coupling for efficient extraction of plasmons to free-space THz radiation requires optimized grating periods $\Lambda \sim 2\pi/q \sim 100$–500 nm, readily fabricable with e-beam lithography.

23. Practical Implementation Considerations.

Magnetic field integration

The integration of transverse magnetic fields in the 0.5–2 T range poses significant technological challenges for compact THz devices. Several strategies can provide on-chip magnetic biasing:

Permanent magnet arrays: Miniaturized NdFeB or SmCo permanent magnets (~ 1–2 mm^3) can generate 0.5–1 T fields at distances of 100–500 μm from the graphene plane. Arrays of such magnets, positioned laterally to the active region, enable field uniformity better than ± 5% over device areas of 10 × 10 μm^2. The main advantages are zero power consumption and thermal stability; however, field reconfigurability is limited.

Integrated electromagnets: Planar spiral coils with 50–100.

turns, fabricated via multi-layer lithography in Cu or Al (thickness ~ 2–5 μm), can produce fields up to ~ 0.3–0.5 T with currents of 100–200 mA. While offering dynamic tunability, these structures introduce Joule heating (~ 50–100 mW) requiring active thermal management. Field uniformity degrades beyond ~ 5 × 5 μm^2 active areas due to finite coil dimensions.

Hybrid configurations: Combining a moderate permanent magnet bias (~ 0.5 T) with a small tunable electromagnet (±0.2 T) provides a compromise between field strength, tunability, and power consumption. This approach enables dynamic control while maintaining compact form factors (< 5 × 5 × 2 mm^3 package).

Field uniformity requirements are stringent: variations ΔB/B > 10%

Table 1
Optimal design parameters for different operational regimes, highlighting trade-offs between emission efficiency, bandwidth, and angular control.

Application	C_s [F/m^2]	f_{cutoff} [THz]	Δ θ_C [deg]
High gain, narrow-band	$(8-10)x10^{-4}$	1.5–2.0	±5°
Balanced performance	$(4-6)x10^{-4}$	2.0–2.5	±10°
Wide bandwidth	$(1-3)x10^{-4}$	2.5–3.0	±20°

across the active graphene area introduce spatial inhomogeneity in Landau level energies, broadening resonances and reducing Q_{Landau} by factors of 2–3. Thermal management is critical, as temperature variations $\Delta T > 20$ K shift the Fermi level via thermal broadening and modify carrier mobility, destabilizing the emission characteristics.

Carrier injection and current stability

The quantum Čerenkov mechanism requires a sustained population of high-energy carriers ($E_i \sim 0.05$–0.10 eV, corresponding to velocities v $\sim v_F$). Several injection schemes can maintain this non-equilibrium distribution::

DC current biasing: Applying a moderate DC voltage (V_{DS} ~0.5–1 V) across the graphene channel (length L ~ 1–5 μm) generates an electric field E_{DC} ~ 104–105 V/m. Carriers accelerate along the channel, acquiring kinetic energy $E_{kin} = e\,E_{DC} \cdot \lambda_{mfp}$, where $\lambda_{mfp} \sim 100$–500 nm is the mean free path. For high-quality graphene with $\tau \sim 1$ ps, this yields E_{kin} ~ 50–100 meV, sufficient for Čerenkov emission. The required current densities are J ~ 103–104 A/ cm^2, corresponding to total currents of ~ 1–10 mA for device areas of $10 \times 10\ \mu m^2$.

Current stability is ensured by the fact that the Čerenkov emission timescale ($\tau_{mfp} \sim 10^{-15}$ s, from $\Gamma \sim 10^{15}\ s^{-1}$) is orders of magnitude shorter than carrier scattering times ($\tau \sim 10^{-12}$ s). This temporal separation allows quasi-continuous replenishment of the hot carrier population via electrical injection, preventing depletion.

The drift velocity model above is consistent with experimentally demonstrated hot-carrier populations in gated graphene under moderate DC bias Boubanga-Tombet et al. [7]. Carrier heating via acoustic phonon scattering occurs on nanosecond timescales, much slower than the femtosecond Čerenkov emission process, ensuring a stable non-equilibrium distribution throughout operation. Optical phonon emission is energetically suppressed under THz drive conditions, since phonon energies (~160–200 meV) greatly exceed the relevant photon energies ($\hbar\,\omega_{\text{THz}} \ll 10$ meV). Velocity saturation effects become relevant only for $E_{DC} > 105$ V/m, outside the parameter range considered here.

Optical pumping: Ultrafast laser pulses (duration ~ 50–100.

fs, wavelength ~ 800 nm) can generate non-equilibrium carrier distributions with effective temperatures T_{eff} ~ 2000–3000 K, corresponding to mean energies ~ 0.2–0.3 eV. While offering transient operation with minimal thermal load, this approach requires external optical sources and synchronization, limiting integration prospects.

Heterostructure tunneling: Van der Waals heterostructures (e.g., graphene/hBN/graphene) with vertically applied bias enable controlled injection of carriers with well-defined energies via resonant tunneling. Energy selectivity ΔE ~ 10–20 meV is achievable, offering precise control of the C erenkov emission spectrum.

Power dissipation in the DC biasing scheme is $P_{diss} = V_{DS} \cdot I \sim$ 0.5–10 mW, manageable with standard microfabrication heat sinking. However, current crowding effects and contact resistance ($R_{contact} \sim$ 100–500 Ω · μm) must be minimized via optimized electrode geometries (e.g., edge contacts, graphenemetal alloy formation).

Fabrication tolerances and Material quality

Device performance critically depends on graphene quality and structural tolerances:

Graphene mobility: Room-temperature mobility $\mu > 10^4\ cm^2$/Vs is required to ensure $Q_{\text{Landau}} > 10$. This necessitates high-quality CVD growth or mechanical exfoliation on hBN substrates, followed by careful transfer processes minimizing contamination and wrinkles. Mobility degradation due to substrate interactions, residues, or grain boundaries reduces τ, broadening Landau resonances and diminishing emission enhancement.

Confinement geometry: The parallel plate spacing (d_A, d_B ~ 10–100 nm) must be controlled to ± 5 nm to maintain capacitance uniformity ΔCs/Cs < 10%. Variations beyond this tolerance introduce spatial inhomogeneity in plasmon phase velocity, distorting the emission angular pattern. Atomic layer deposition (ALD) of dielectric spacers (e.g., Al2O3, HfO2) offers the required thickness control.

Fermi level stability: Electrostatic doping via back-gate voltages (V_{BG} ~ 0–50 V) sets the Fermi level E_F with precision Δ E_F ~ 5–10 meV. However, charge trapping in dielectrics, ambient doping (H2O, O2 adsorption), and hysteresis effects can shift E_F by ~ 50–100 meV over timescales of minutes to hours. Encapsulation in inert environments (e.g., hBN capping, vacuum packaging) stabilizes E_F to < 10 meV over operational lifetimes.

Grating coupling and extraction efficiency

Efficient conversion of confined plasmons to free-space THz radiation requires optimized grating couplers. The grating period Λ must satisfy the phase-matching condition:

$$\Lambda = \frac{2\pi}{q - k_0 \sin\theta_{out}}, \tag{28}$$

where q is the plasmon wavevector and θout is the desired output angle. For f ~ 1 THz and q ~ 0.02–0.05 rad/nm, optimal periods are Λ ~ 200–400 nm.

Fabrication via electron-beam lithography enables precise control of grating duty cycle (~ 50%), depth (~ 50–100 nm), and periodicity (ΔΛ/Λ < 5%). Metal gratings (Au, Al) patterned directly on the graphene surface provide coupling efficiencies ηcouple ~ 10–30%, extracting a significant fraction of plasmonic power as directional THz beams.

Second-order gratings (Λ ~ 400 − 800 nm) offer relaxed fabrication tolerances while maintaining ηcouple > 5%, suitable for proof-of-concept demonstrations. For applications requiring high directionality (beamwidth < 10), blazed or chirped grating profiles optimize the angular emission pattern.

The coupling efficiency ηcouple ~ 10–30% can be estimated from the grating diffraction integral for first-order metal gratings (Λ ~ 200–400 nm, depth h ~ 50–100 nm), consistent with experimental values reported for graphene plasmon grating couplers. The net device output power is Pout = ηcouple · Pplasmon, so improving coupling efficiency directly scales THz output without modifying the intrinsic plasmonic gain. Resonant cavity configurations (Fabry–Perot between two gratings) can raise ηcouple above 50%, bringing the estimated output power to the ~ 1 μW level detectable by standard THz bolometers.

Thermal management

Combining electrical injection ($P_{\text{elec}} \sim 1$–10 mW) and magnetic field generation (P_{mag} ~ 50–100 mW for electromagnets) results in total dissipation P_{total} ~ 50–110 mW within millimeter-scale packages. Without adequate heat sinking, this produces temperature rises ΔT ~ 50–100 K, shifting E_F, reducing μ, and broadening Landau levels.

Integration of micro-channel heat sinks, diamond heat spreaders, or thermoelectric coolers maintains junction temperatures $T_{\text{junction}} < 350$ K, ensuring stable operation. For cryogenic applications (e.g., quantum information processing), operation at T ~ 77 K (liquid nitrogen) or T ~ 4 K (liquid helium) dramatically enhances Q_{Landau} (by factors of 5–10) and reduces thermal broadening, at the cost of increased system complexity.

A complete power budget for a representative device (10 × 10 μm2 active area, permanent NdFeB magnet, DC bias injection) is as follows. Carrier injection dissipates $P_{\text{bias}} \sim 1$– 10 mW; magnetic field generation with permanent magnets requires zero additional power. The estimated useful THz output via grating outcoupling is Pout ~ 0.1–1 μW, giving a wall-plug efficiency $\eta_{\text{WP}} \sim 10 - 4$, comparable to photoconductive THz emitters operating at room temperature. While this is lower than

cryogenic QCLs, the proposed device does not require cooling, operates at DC bias below 1 V, and provides magnetic tunability of emission direction, frequency, and polarization on a single chip.

Table 2 consolidates the key design parameters and their feasibility assessment.

Applications and Future Directions

The resonant enhancement mechanism enables compact magnetically-tunable THz amplifiers with gain of 20–30 dB (from $\Gamma^B/\Gamma^0 \sim 10$–100), bandwidth of 0.5–3.5 THz (magnetically tunable), steering of 360° azimuthal control, and footprint $< 10 \times 10\ \mu m^2$.

The non-reciprocal magnetoplasmon propagation enables integrated THz circulators and on-chip circulators and isolators without ferrites, critical for THz transceivers and imaging systems. Selective excitation of specific Landau levels produces chiral light sources with circularly polarized THz emission, useful for chiral molecule spectroscopy, spin-sensitive detection, and quantum information processing.

Combining electrostatic ($\boldsymbol{E_F}$) and magnetostatic (B) control enables multi-functional devices with simultaneous tuning of frequency (via $\boldsymbol{E_F}$), direction (via B), and polarization (via B and grating design). Future work should explore the strongfield regime ($\omega c > \omega p$), quantum Hall edge state coupling, time-modulated magnetic fields for frequency conversion, and integration with van der Waals heterostructures.

Experimental verification of the predicted Čerenkov plasmonic emission can proceed through several complementary approaches. Plasmon-assisted THz free-space emission via grating outcoupling ($\Lambda \sim$ 200–400 nm) is expected to yield detectable output powers of $\sim$ 0.1–1 μW, within the sensitivity of standard THz bolometric detectors. Direct near-field imaging via THz s-SNOM can resolve the predicted plasmon wavelength ($\lambda p \sim$ 130–300 nm at 1 THz) and detect the magnetic field-induced splitting of the two chiral branches as two distinct spatial periodicities. Transport spectroscopy under DC bias can identify the Čerenkov threshold via a nonlinear feature in dI/dV at VDS $\sim$ 0.3–0.5 V. Polarization-resolved THz time-domain spectroscopy can detect the predicted Faraday rotation ($\theta F \sim$ 15–30∘ at B = 1 T), providing direct evidence of non-reciprocal magnetoplasmon behavior.

Table 3 places the proposed device in context with established THz source technologies.

Summary and conclusions

We have presented a comprehensive theoretical framework for quantum Čerenkov emission in confined graphene structures, demonstrating emission rate enhancements exceeding an order of magnitude compared to unconfined geometries. The extension to include transverse magnetic fields reveals rich physics: Landau level quantization, magnetoplasmon formation, directional emission control, resonant enhancement, and non-reciprocal propagation.

The combination of metallic confinement and magnetic field control provides unprecedented tunability of THz emission characteristics. Emission rates reach $\sim 10^{15}\ s^{-1}$, with femtosecond timescales ensuring stability. Magnetic fields of 1–2 T enable beam steering over 360°, frequency range extension by ~75%, and resonant enhancement factors of 10–100.

These findings establish graphene-based quantum Čerenkov emitters as promising platforms for next-generation THz technology, including magnetically-tunable amplifiers, integrated circulators, chiral light sources, and multi-functional photonic devices. The ability to dynamically control emission direction, frequency, and polarization on a single chip opens pathways toward compact, versatile THz systems for communications, spectroscopy, and imaging.

Table 2
Key implementation parameters and feasibility.

Parameter	Value	Feasibility notes
Mag. field B	0.5–2 T	NdFeB/SmCo magnets
Mobility μ	$> 10^4 cm^2/Vs$	hBN-encapsulated graphene
Relax. time τ	~ 1 ps	$\tau = \mu E_F/(ev_F^2)$
Spacing d	10–100 nm	ALD; ± 5 nm control
Current density J	$10^3 - 10^4 A/cm^2$	Total current < 10 mA
Joule heating	1–10 mW	ΔT < 20 K
Output P_{out}	0.1–1 μW	Grating coupling, η ~ 10–30%
WP efficiency	$\sim 10^{-4}$	Cf. photocond. antenna

Table 3
Performance comparison: this work vs. QCL and photoconductive antenna (PA). Output power values are representative literature ranges.

	This work (B = 0)	This work (B = 2T)	QLC (cryo.)	Photocond. antenna
Freq. (THz)	0–2	0–3.5	1–5	0.1–3
Tuning	$\boldsymbol{E_F}$	B+$\boldsymbol{E_F}$	10%	broad
Steering	–	360°	–	–
T (K)	300	300	4–100	300
Footprint	$<100\ \mu m^2$	$<100\ \mu m^2$	cm^2	mm^2
$\boldsymbol{P_{out}}$	0.1–1 μW	0.1–10 μW	1–100mW	1–100 μW

CRediT authorship contribution statement

Luca Pierantoni: Writing – review & editing, Writing – original draft, Software, Resources, Project administration, Methodology, Investigation, Funding acquisition, Formal analysis, Conceptualization. **Tullio Rozzi:** Validation, Supervision, Conceptualization. **Davide Mencarelli:** Writing – review & editing, Validation, Software, Funding acquisition, Conceptualization. **Gian Marco Zampa:** Validation, Supervision. **Alessandro Toscano:** Writing – review & editing, Supervision. **Michela Longhi:** Writing – review & editing, Validation, Supervision, Software, Resources, Methodology, Investigation, Data curation.

Declaration of competing interest

The authors declare that they have no known competing financial interests or personal relationships that could have appeared to influence the work reported in this paper.

Acknowledgements

This work was supported by the European Union (Horizon EIC, 2022, Project No. 101099552, 'Nano-scale Development of Plasmonic Amplifiers Based on 2D Materials' (PLASNANO)) and by the European Union under the NextGenerationEU programme, within the Italian National Recovery and Resilience Plan (NRRP), Mission 4, Component 2, Investment 1.3, Project 'Telecommunications of the Future' (PE00000001 – RESTART), CUP B53C22003970001.

Data availability

Data will be made available on request.

References

[1] Dhillon S, Vitiello MS, Linfield EH, Davies AG, Hoffmann MC, Booske J, et al. J Phys D Appl Phys 2017;50:043001.
[2] Woessner A, Lundeberg MB, Gao Y, Principi A, Alonso-González P, Carrega M, et al. Nat Mater 2015;14:421.
[3] Zhang D, Huang X, Zhang Z, Wang Z, Wang Z, Yu Y, et al. Nature 2022;611:55.

[4] Jadidi MM, Sushkov AB, Myers-Ward RL, Boyd AK, Daniels KM, Gaskill DK, et al. Nano Lett 2015;15:7099.
[5] Mir SH, Yadav VK, Singh JK. ACS Omega 2020;5:14203.
[6] Gosling JH, Makarovsky O, Wang F, Akhter ND, Ali R, Fordham BN, et al. Commun Phys 2021;4:30.
[7] Boubanga-Tombet S, Knap W, Yadav D, Satou A, But D, Popov V, et al. Phys Rev X 2020;10:031004.
[8] Mencarelli D, Bellucci S, Sindona A, Pierantoni L. J Phys D Appl Phys 2015;48:465104.
[9] Mencarelli D, Nishina Y, Ishikawa A, Pierantoni L, Bellucci S. Opt Data Process Storage 2017;3:89.
[10] Kaminer I, Kooi SE, Shiloh R, Zhen B, Yang Y, Joannopoulos JD, et al. Phys Rev X 2016;6:011006.
[11] Kaminer I, Nemirovsky J, Rechtsman M, Bekenstein R, Segev M. Nat Commun 2016;7:11880.
[12] Zampa GM, Mencarelli D, Pierantoni L, Rozzi T. Appl Phys Lett 2024;124:054101.
[13] Pierantoni L, Mencarelli D, Rozzi T, editors. Graphene Science Handbook: Electrical and Optical Properties. Boca Raton: CRC Press; 2015. p. 85–100.
[14] Pierantoni L, Mencarelli D, Bozzi M, Moro R, Moscato S, Perregrini L, et al. IEEE Trans Microw Theory Tech 2015;63:2491–7.
[15] Ginzburg V. Zh. Eksp. Teor. Fiz. 1940;10:589.
[16] Novoselov KS, Geim AK, Morozov SV, Jiang D, Katsnelson MI, Grigorieva IV, et al. Nature 2005;438:197.